

## Pinhole camera for electron beam size diagnostic at storage ring with an ultralow emittance

Andrei Trebushinin<sup>1</sup>,\* Gianluca Geloni, and Svitozar Serkez  
European XFEL, 4, Holzkoppel Street, 22869 Schenefeld, Germany

Ruslan Khubbutdinov and Evgeny Saldin  
Deutsches Elektronen-Synchrotron, Notkestraße 85, 22607 Hamburg, Germany



(Received 27 December 2023; accepted 22 February 2024; published 8 March 2024)

In this work, we propose to use a pinhole camera at high photon energies, specifically 200–300 keV, to measure ultra-small electron beam size by means of bending magnet radiation. We show that there is a sufficient photon flux at the detector position. Our theoretical analysis includes an examination of the applicability of the van Cittert-Zernike theorem for the bending magnet radiation generated by an ultralow emittance electron beam and a detailed analysis of the imaging properties of rectangular pinhole cameras. This led us to practical, universal formulas. We identify the optimal aperture size and resolution of the camera in the given geometry. The theoretical findings are further substantiated by wavefront propagation numerical simulations of partially coherent radiation. This study serves both as a practical guide for optical engineering and an educational resource for explaining the imaging properties of pinhole cameras.

DOI: [10.1103/PhysRevAccelBeams.27.032802](https://doi.org/10.1103/PhysRevAccelBeams.27.032802)

### I. INTRODUCTION

Advancements in the magnetic lattice design for storage rings [1], along with the rapid design and construction of next-generation synchrotron radiation (SR) light sources [2,3], and cited within [4], have significantly reduced the transverse electron beam size with respect to third-generation light sources. This leads to a clear benefit in terms of (spectral) brightness and coherence properties [5,6] for users' applications [7,8] but imposes tight requirements on electron beam diagnostic techniques based on synchrotron radiation, in particular, those that utilize pinhole cameras.

The imaging properties of pinhole cameras have been known since ancient times and are now routinely used to visualize the objects at different wavelengths. In the case of x rays, they have served as robust and effective tools for electron beam size measurements throughout the development years of SR sources, with recent applications [9–11]; a review table can be found in [12], numerical analyses of the spatial resolution of x-ray pinholes were conducted in [9,11] with SRW code [13,14] and with comparisons to measurements presented in [15]. Incoherent imaging of

objects as small as the transverse size of the electron beam in the modern diffraction-limited storage rings (with low emittance on the order of 20 pm rad) requires the use of shorter wavelengths compared to previously proposed setups to achieve sufficient resolution. The reason being the width of the point-spread function is proportional to the square root of the radiation wavelength [16], Eq. 319.

Incoherent imaging enables the direct measurement of the source size distribution without being influenced by the radiation distribution from a single electron emitter. In the case presented here, the setups necessitate the installation of a dedicated radiation source, for example, a three-pole magnetic chicane with a high magnetic field. In contrast, techniques that rely on the partially coherent properties of radiation, wherein the correlation function retains information about the electron beam size, usually do not require the installation of a separate radiation source. However, data interpretation and the retrieval of electron beam size may be more complex. An overview of SR-based diagnostics for measuring the transverse size of the electron beam can be found in [12,17]. Furthermore, there exist more subtle techniques that leverage both imaging and partially coherent properties of radiation to determine the electron beam size, as demonstrated in [18,19].

In this paper, we propose a pinhole camera setup using higher than usual photon energies, up to 200–300 keV, generated by a central magnet of a magnetic chicane, so it can be considered as the bending magnet radiation. Our research focuses on optimizing the resolution capabilities of this setup. For this, we studied the imaging characteristics of a rectangular pinhole camera with wave optics

\*andrei.trebushinin@xfel.eu

Published by the American Physical Society under the terms of the *Creative Commons Attribution 4.0 International* license. Further distribution of this work must maintain attribution to the author(s) and the published article's title, journal citation, and DOI.

approaches based on [16]. This study is augmented by examining the applicability of the van Cittert-Zernike theorem in the case of bending magnet radiation. As a result, we present analytical design formulas and an expression for the point spread function of a rectangular pinhole camera and compare these results with numerical simulations. We validate these theoretical derivations with wavefront propagation simulations in the OCELOT toolkit [20,21] using the Gaussian random fields approach [22] for simulating partially coherent radiation. We conclude our paper with the calculation of photon flux to demonstrate that it is sufficient for electron beam diagnostics purposes.

## II. THEORY

In this section, we first provide proof of the applicability of the van Cittert-Zernike theorem within the parameter space of our problem, with a quantitative estimation presented in Sec. II A. Then we outline the requirements for an aperture to function as a pinhole and to form an image. We conclude this discussion by presenting calculations for the optimal parameters of a pinhole camera to achieve the best possible resolution. Our findings include simple design formulas and universal plots that can be employed in the optical engineering of pinhole cameras. These results are further supplemented by wavefront propagation simulations of pinhole optics.

### A. Applicability of the van Cittert-Zernike theorem

Let us consider the applicability of the van Cittert-Zernike theorem to bending magnet radiation at a frequency much higher than its critical frequency. The theorem connects the radiation distribution of the source with the coherence properties in the far zone. It can be stated as follows: The modulus of the spectral degree of coherence between two points in the far field of an incoherent source is equivalent to the two-dimensional Fourier transform of the source intensity distribution. The validity of this theorem forms the basis for applying incoherent imaging theory in the case of a pinhole camera.

Within statistical optics, SR is described as a Gaussian random process. An important consequence of this is that the higher-order correlation functions of the process can be expressed in terms of the first-order correlation function ( $G$ ) with the help of the moment theorem. As a result, knowing the second-order correlation function in the space-frequency domain is all one needs to completely characterize the signal from a statistical viewpoint.

The following definition holds:

$$G(\vec{r}_1, \vec{r}_2, \omega_1, \omega_2) = \langle E(\vec{r}_1, \omega_1) E^*(\vec{r}_2, \omega_2) \rangle, \quad (1)$$

where brackets indicate ensemble averaging,  $E$  is the electric field (considered as a scalar, i.e., limiting ourselves to a given polarization component),  $\vec{r}$  is the transverse

coordinate, and  $\omega$  is the radiation frequency. By ensemble averaging in the case of SR, we mean averaging of radiation samples from different electron bunches that are considered to share the same phase-space distribution.

Since SR radiation constitutes an ensemble of pulses of finite duration, it is an intrinsically nonstationary statistical process. However, in most practical cases, the electron beam defines the duration of the radiation pulses ( $\sigma_t$ ), which is the order of several picoseconds (corresponding to a few millimeters length), while the coherence time is related to the formation length of the radiation ( $L_f$ ). For example, for bending magnet radiation at the critical wavelength  $\lambda_c$ , coherence time is given simply by ( $\tau_c \approx L_f(1 - v/c) \sim \lambda_c/c$ ), where  $\gamma = 1/\sqrt{1 - v^2/c^2}$  is the Lorentz factor. It is evident that for x-ray sources,  $\tau_c \ll \sigma_t$ , resulting in a very large number of spikes, classifying this type of source as quasistationary and granting applicability of the Wiener-Khinchin theorem. In this case,  $\langle E(\vec{r}, \omega) \rangle$  varies negligibly at the spike width scale  $\sim 1/\sigma_t$ . Hence, we can simplify the correlation function to

$$G(\vec{r}_1, \vec{r}_2, \omega) = \langle E(\vec{r}_1, \omega) E^*(\vec{r}_2, \omega) \rangle. \quad (2)$$

This function is known as cross-spectral density.

Before continuing, we introduce the notion of spectral degree of coherence  $g(\vec{r}_1, \vec{r}_2)$ , as

$$g(\vec{r}_1, \vec{r}_2) = \frac{G(\vec{r}_1, \vec{r}_2)}{[G(\vec{r}_1, \vec{r}_1)G(\vec{r}_2, \vec{r}_2)]^{1/2}}, \quad (3)$$

where, for the notation simplicity, we omitted the dependence on  $\omega$ . The function  $g(\vec{r}_1, \vec{r}_2)$  is normalized to unity by definition.

The concept of quasistationarity in the time domain is the temporal analogy of quasihomogeneity in the spatial domain. A quasihomogeneous source obeys the assumption that  $\langle |E(\vec{r})|^2 \rangle$  varies slowly on the scale of the transverse coherence length, which is the effective width of the spectral degree of coherence  $g(\Delta\vec{r})$ . Because of this, for quasihomogeneous sources, the following approximation holds

$$G(\vec{r}, \Delta\vec{r}) = I(\vec{r})g(\Delta\vec{r}), \quad (4)$$

where now  $I(\vec{r})$  is proportional to the radiation intensity distribution at the source and where  $\Delta\vec{r} = \vec{r}_2 - \vec{r}_1$ .

A significant special case follows from Eq. (4) when  $g(\Delta\vec{r})$  has a spatial width comparable to the radiation wavelength. In practical calculations, it is possible to approximate  $g(\Delta\vec{r})$  with a two-dimensional Dirac delta function  $\delta(\Delta\vec{r})$  even when the optical system has much poorer resolution than the wavelength [23]. Thus the expression for the cross-spectral density can be approximated by

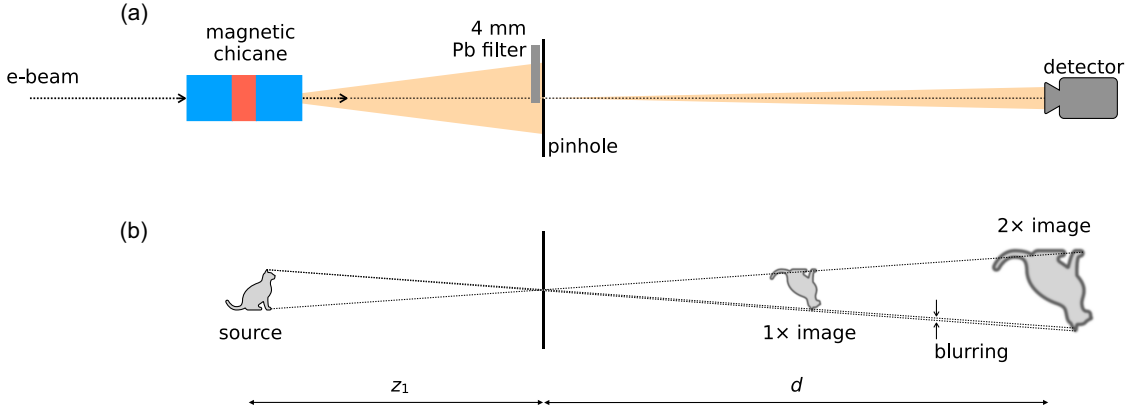


FIG. 1. Pinhole camera imaging setup: (a) outline of the proposed setup and (b) a visual explanation of the imaging properties of a pinhole in the ray-tracing approximation. Image blurring represents the actual blurring.

$$G(\vec{r}, \Delta\vec{r}) = I(\vec{r})\delta(\Delta\vec{r}), \quad (5)$$

This kind of source is transversely incoherent. Both types of sources: Eqs. (4) and (5) follow the van Cittert-Zernike theorem. The original theorem was formulated for incoherent sources in [24,25], followed by the generalized version that was presented in [26,27].

Here we provide a quantitative estimate of the applicability of the theorem in the case of bending magnet radiation. We can always express the diffraction-limited size and the divergence of the radiation through SR formation length ( $L_f$ ) as  $\sigma_r \sim \sqrt{\lambda/L_f}$  and  $\sigma_r \sim \sqrt{\lambda L_f}$ . This always guarantees that

$$\sigma_r \sigma_r \sim \lambda. \quad (6)$$

In our case of small wavelengths, we consider the asymptotic limit with a large  $y = \lambda_{\text{phc}}/\lambda_{\text{ph}}$  and obtain  $\sigma_r \sim 1/(\sqrt{y}\gamma)$ , where  $\lambda_{\text{phc}} \sim R/\gamma^3$  [28]. Using the relation in Eq. (6), we obtain that  $L_f \sim R/\gamma$ . Substituting this into the expression for the diffraction-limited radiation size results in  $\sigma_r \sim R/(\sqrt{y}\gamma^2)$ . To estimate the beam size, we use  $R \approx 10$  m,  $y \approx 10$ , and  $\gamma = 12000$ . This yields  $\sigma_r \sim 20$  nm. We see that this size is much smaller than the size of the electron beam, and thus we are in the quasihomogeneous asymptotic regime and can safely apply the van Cittert-Zernike theorem.

## B. Rectangular pinhole camera

In the following analysis, we consider the behavior of x-ray pulses impinging on a rectangular pinhole, although our results are applicable to any wavelength. Upon applying similarity techniques, only one dimensionless parameter determines the characteristics of the pinhole camera: the Fresnel number.

First, we define a pinhole camera as an optical element that is typically associated with the following requirements: (i) The pinhole must be situated in the far zone from the

source. This condition is necessary for relating the cross-spectral density function of the imaged object in the far zone to the source's intensity distribution. This requirement stems from the van Cittert-Zernike theorem. (ii) The pinhole size must be larger than the radiation coherence length, ensuring the aperture does not alter the cross-spectral density function. (iii) The source size must be larger than the aperture size to achieve adequate resolution.

These three conditions are general requirements for an aperture to function as a pinhole and to form an image of the source. We present the outline of the pinhole imaging setup in Fig. 1. In Figs. 2 and 3, we present snapshots of the radiation as seen from a perfect monochromator at a specific frequency  $\omega$ . This representation remains general because, in the frequency domain, different spikes in the spectrum are statistically independent and can be analyzed separately.

After propagating to the far zone, the radiation from the source undergoes spatial filtering by the pinhole. The pinhole ensures that the coherence properties of the

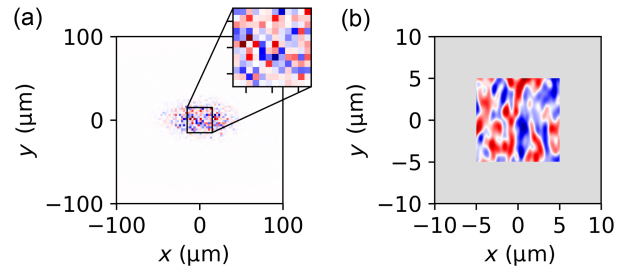


FIG. 2. (a) A single statistical realization of the monochromatized radiation field at the source, characterized by a Gaussian distribution with a standard deviation of the transverse size of  $20 \times 10 \mu\text{m}^2$ . This realization includes a noise structure that models the source's incoherence. (b) A single statistical realization after propagation through a  $10 \times 10 \mu\text{m}^2$  aperture. In these images, false colors represented by red and blue indicate the positive and negative amplitudes of the slowly varying envelope of the electric field.

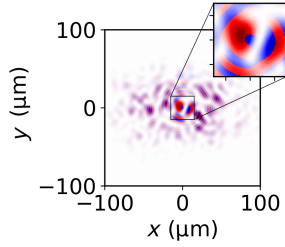


FIG. 3. A single shot image taken after the pinhole in the far zone. The spiky structure indicates the acquired coherence of the radiation that occurred upon free space propagation. Note quadratic phase front curvature, visible as rings of alternating false color.

radiation are preserved while it significantly alters the spatial frequency distribution ( $k_x, k_y$ ), or equivalently, the angular distribution. This effectively creates a secondary source, preserving the coherence length in the far zone along with all information about the source size. Consequently, an image of the source forms in the far zone beyond the pinhole. In the following section, we will detail the optimal parameters for the pinhole camera and elaborate on the first and second conditions previously discussed.

### C. Optimal parameters for a rectangular pinhole

We observe that the pinhole point spread function can be factorized and may be presented as multiplication of two one-dimensional line spread functions for each direction:  $l_{ps} = l_{ps_x} \cdot l_{ps_y}$ , where line spread functions are written as [16], Eq. 313

$$l_{ps_{x,y}}(\Omega, y') = \int_{-1}^1 d\xi \frac{\sin[2(\xi\Omega + y'\sqrt{\Omega})(1 - |\xi|)]}{\xi\Omega + y'\sqrt{\Omega}}, \quad (7)$$

where  $\xi$  is the transverse coordinate normalized by the aperture size. The point spread function is determined solely by the dimensionless parameter  $\Omega = a^2/(\lambda z_{\text{eff}})$ , where  $z_{\text{eff}} = z_1 d/(z_1 + d)$ ,  $z_1$  is the distance from the source to the pinhole,  $d$  is the distance from the pinhole to the image plane, and  $a$  is the half-width of the aperture.

To optimize pinhole imaging performance and achieve higher resolution, one should minimize the width of the distribution given by Eq. (7) with respect to the  $\Omega$  parameter. Figure 4 presents a scan of the line spread function as a function of  $\Omega$ . Due to the presence of sinc-function side lobes, the shape of the line spread function is nontrivial. Given that its full width at half maximum may not clearly indicate the best performance, selecting the optimum  $\Omega$  parameter is a subjective matter. We chose  $\Omega = 4.5$ . This choice ultimately leads to the following formula for the optimal pinhole camera aperture size:

$$a^2 \approx 4.5\lambda z_{\text{eff}}. \quad (8)$$

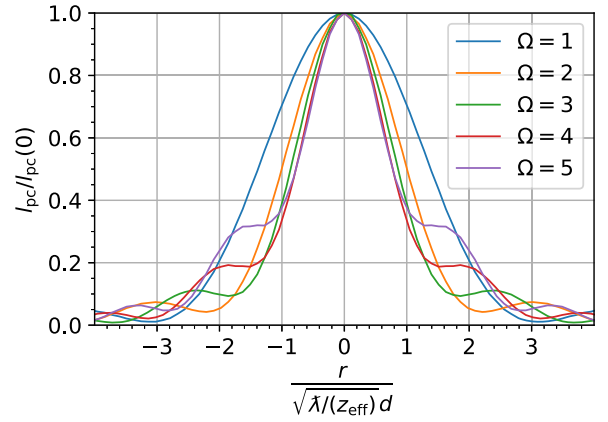


FIG. 4. Line spread functions for various  $\Omega$ . We may choose the optimum as  $\Omega = 4.5$ , while other choices can be equally valid as in the region  $2 < \Omega < 5$  we have almost the same width of the main peak and slightly different “wings.” Here we found an optimum between defocusing aberration and diffraction effects.

This corresponds to an optimum between defocusing aberrations and diffraction effects. For a detailed explanation of the limits of large and small  $\Omega$ , we refer the reader to [16].

We analyzed the imaging problem numerically using the OCELOT toolkit [21], employing a model where a point source propagates through an optical system. This simulation yields a point spread function at the pinhole when the aperture is set to its optimal size. The results are presented in Fig. 5.

We also studied the evolution of the point spread function downstream of the aperture, as illustrated in Fig. 6(a). After normalizing the spatial units, as depicted in Fig. 6(b), the relative resolution stabilizes to its minimum, approximately 0.3 times the diffraction length ( $\lambda z/a^2$ ), from the slit, as also noted in [9]. We provide an expression for the full width at the half maximum of the line spread function:

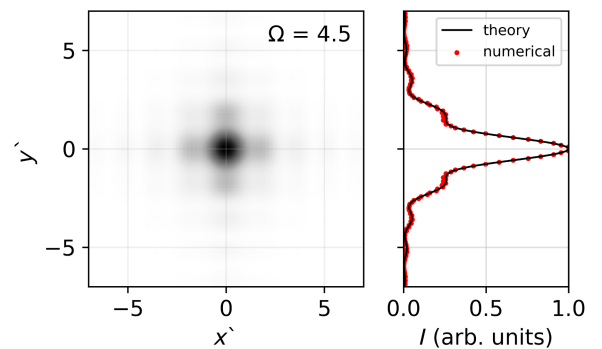


FIG. 5. Comparison of the analytical point spread function with numerical calculations for  $\Omega = 4.5$ .

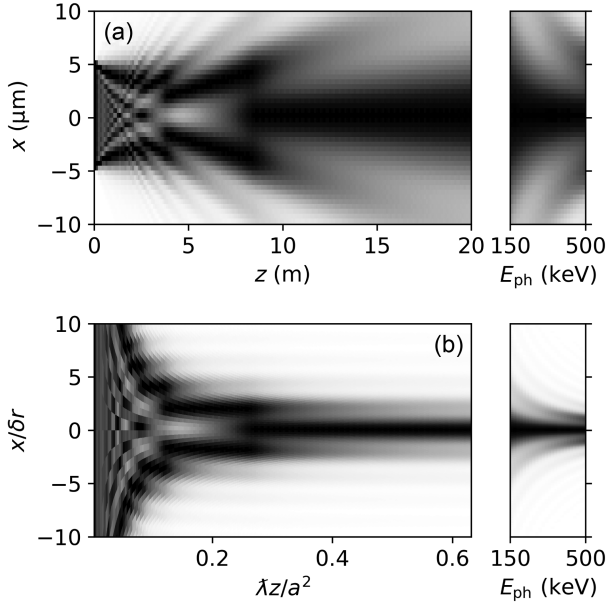


FIG. 6. Line spread function evolution after the pinhole with the optimal size of  $\Omega = 4.5$  or  $10 \times 10 \mu\text{m}^2$  at 250 keV. In (a), the axes are presented in physical units, while in (b), the axes are in dimensionless units. The horizontal axis is in units of the diffraction length, where 0.63 corresponds to the image location at 20 m. The vertical axis is expressed in units of relative resolution, as derived from the expression in Eq. (9). The right-hand side of (a) and (b) illustrates the variation of the line spread function with respect to energy. Interestingly, the distribution undergoes a series of abrupt transitions before reaching the far zone, indicating that the transition from the near zone to the far zone is not smooth but rather abrupt.

$$\delta r \simeq 1.5 \sqrt{\frac{\lambda}{z_{\text{eff}}}} d. \quad (9)$$

As evident from the preceding discussion, rectangular geometry serves as a demonstrative approach for teaching the optics of a pinhole camera. Explaining the concept with a rectangular aperture helps to demonstrate the properties of the diffracted field, eliminating the need for complex derivations.

#### D. Numerical simulations

Wavefront simulations based on the propagation of partially coherent fields were investigated in [22]. We used this technique to model the bending magnet radiation. We generated numerous ( $10^4$ ) statistical realizations of the radiation field, as illustrated in Figs. 2(a) and 3, and ensemble-averaged them to obtain an experimentally observable distribution, as would be observed on a beam-line equipped with a conventional monochromator. In Figs. 7 and 8, we illustrated how the size of the point spread function compares to the size of the image. We utilized the parameters listed in Table I.

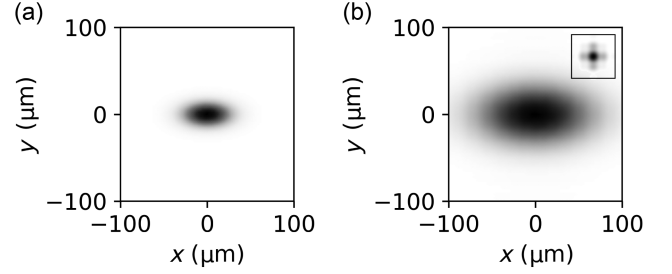


FIG. 7. (a) Source distributions and (b) its twofold magnified image, convolved with the point spread function (provided to scale in an embedded inset).

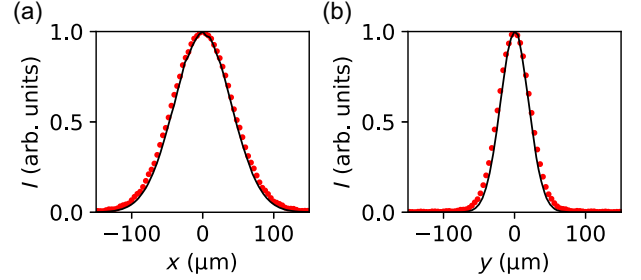


FIG. 8. Image (dashed line) and the source distribution (solid line), which is 2 times magnified for comparison. Slice over  $x = 0$  and  $y = 0$  from Fig. 7 for each direction correspondingly.

We roughly estimated the expected blurring of the size of the image beam size using an approximate formula

$$\sigma_i = \sqrt{4\sigma_e^2 + \sigma_{\text{psf}}^2}. \quad (10)$$

This formula underestimates the actual resulting size because it assumes that widths sum up quadratically, which is only true for Gaussian distributions. However, in this case, we are dealing with a non-Gaussian distribution of the point spread function, as observed in Fig. 4. The factor of 4 originates from the specific geometry of the pinhole camera. Based on a Gaussian fit,  $\sigma_{\text{psf}}$  is estimated to be

TABLE I. Simulation parameters.

Parameter	Value
Natural emittance ( $\epsilon_{0_x} \times \epsilon_{0_y}$ )	$20 \times 5$ (pm rad) <sup>2</sup>
Beta function ( $\beta_{x,y}$ )	20 m
Beam size ( $\sigma_x \times \sigma_y$ )	$20 \times 10 \mu\text{m}^2$
Beam energy ( $E_{\text{beam}}$ )	6 GeV
Photon energy ( $E_{\text{ph}}$ )	250 keV
Source to pinhole ( $z_1$ )	10 m
Pinhole to image ( $d$ )	20 m
Pinhole size ( $a$ )	5 $\mu\text{m}$
Point spread function:	
FWHM	10.3 $\mu\text{m}$
$\sigma_{\text{psf}}$	6.7 $\mu\text{m}$

TABLE II. Image sizes.

	$\sigma_i, \mu\text{m}$ [(Eq. (10))]	$\sigma_i, \mu\text{m}$ (simulation)
$\sigma_x = 20 \mu\text{m}$	40.6	42.3
$\sigma_y = 10 \mu\text{m}$	21.1	22.3

6.7  $\mu\text{m}$  from the simulation. We present a comparison of this estimation with the simulation results in Table II.

### III. PROPOSED SETUP

In this section, we propose the conceptual design of a setup to diagnose the electron beam size. We suggest a three-pole, 1-m-long magnetic chicane, schematically depicted in Figs. 1 and 9, to serve as a synchrotron radiation source. The device features a single yoke with coils powered by a single power supply. The magnetic field in the outer compensatory coils is three times lower than that in the central coil. The design's advantages include its compactness and low cost. The SR background from the outer magnets of the chicane and other storage ring bending magnets is negligibly small, as we operate at large values of  $y = \lambda_{\text{ph}_c}/\lambda_{\text{ph}}$ . This kind of device should be installed in a zero-dispersion section of the storage ring. This placement is crucial to prevent an increase in beam emittance.

In the hard x-ray range, a rectangular pinhole can be easily formed using a combination of two perpendicular conventional slits. It is important to note that the slits should be sufficiently thick to block 300-keV-order hard x-ray light.

The SR emitted by the central pole is filtered through a 4-mm-thick lead filter to narrow down the radiation bandwidth. We need this filtration to mitigate the effects of dispersion at the lower end of photon energies. The exponentially decaying tail of the SR spectrum, combined with the transmission characteristic of the filter, effectively creates a bell-shaped spectrum with a 150 keV bandwidth and 250 keV central energy, as seen in Fig. 11. The filter thickness is optimized for sufficient photon flux at the detector and acceptable resolution based on the radiation bandwidth. We estimate the photon flux to be around  $8 \times 10^7$  photons/s for a 4-mm-thick Pb filter, chicane magnetic field of 1.7 T, and 100 mA electron beam.

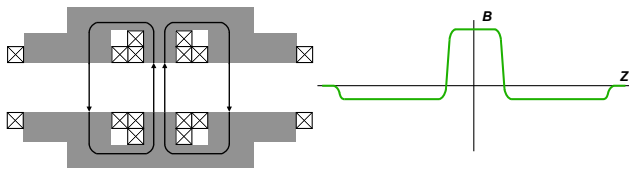


FIG. 9. Magnetic chicane for the proposed x-ray pinhole camera. The magnetic field of the central pole is about 1.7 T. The overall length of the device is 1 m.

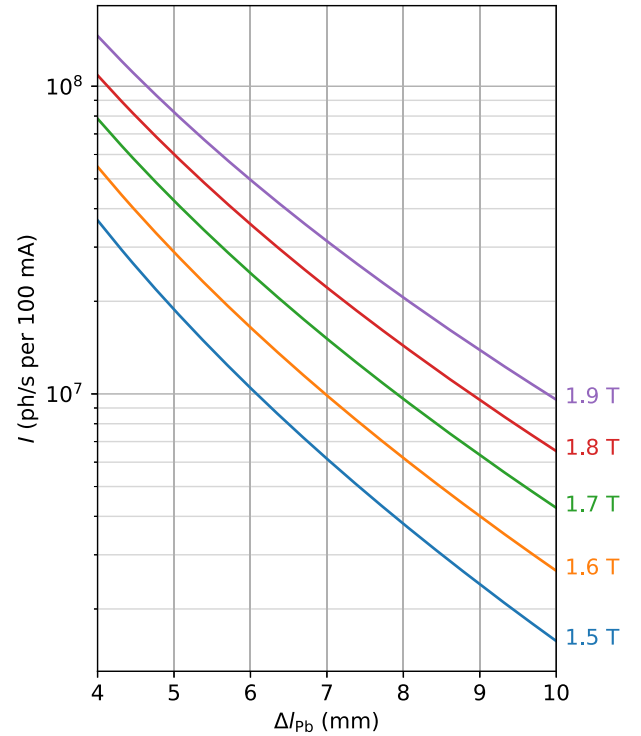


FIG. 10. Estimation of the photon flux through the pinhole from a 6 GeV electron beam as a function of the thickness of the Pb filter, plotted for different amplitudes of the magnetic field of the central magnet of the chicane.

Figure 10 provides an estimation of the photon flux for magnetic fields ranging from 1.5 to 1.9 T.

### IV. DISCUSSION

In this section, we address important considerations for implementing the pinhole camera in a real facility, which were not covered in the main body of this paper. First, one needs to consider that to obtain accurate results from the

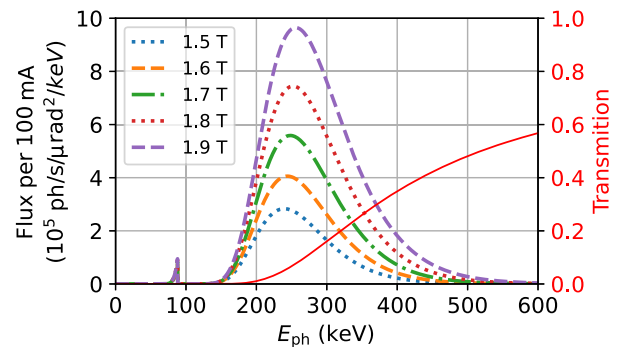


FIG. 11. On-axis spectrum of synchrotron radiation upon spectral filtering with 4 mm lead plate. We provide the distribution for different magnetic field strengths of the central pole, assuming a 6 GeV electron beam and with the red line the transmission characteristic of 4 mm of Pb. Calculations are made with SPECTRA code [30].

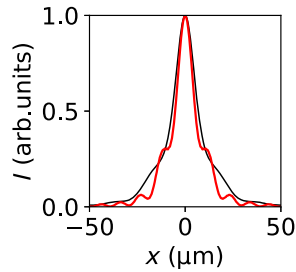


FIG. 12. Comparison of the line spread functions for monochromatic light (red line) and averaged over the whole energy range (black line) presented in Fig. 11 with green line.

measured images, one must perform a deconvolution operation. This operation uses the point spread function described earlier in this paper. Moreover, it is crucial to consider the broad spectrum of radiation passing through the pinhole, as illustrated in Fig. 11. To address this, one must calculate a weighted average of the point spread over the spectrum and perform a deconvolution operation using this average. We present this in comparison to the line spread functions for 250 keV in Fig. 12. The variation of the line spread functions within this energy range is depicted in the right subplot of Fig. 6. The FWHM of the spectrum-averaged line spread function increases from 10.3  $\mu\text{m}$  for monochromatic radiation to 13.7  $\mu\text{m}$ . The subsequent step in data analysis involves deconvolution using the point spread function of the x-ray camera employed in the experiment, as discussed in [9].

Another important question to address is the design of an appropriate detector for the proposed setup. Given these stringent requirements, one may use indirect detectors that convert x-ray photons to the visible range using a scintillator. For high conversion efficiency of the scintillator, materials with a high atomic number ( $Z$ ) are preferred, such as lutetium compounds, such as  $\text{Lu}_2\text{O}_3:\text{Eu}$ , as suggested in [31]. A scintillator made from such materials will generate a sufficient number of photons to be detected by a standard industrial camera and associated optics, as noted by [31]. The photon flux for a specific detector can be readily calculated using data from Fig. 11.

## V. CONCLUSION

In this paper, we discussed the applicability of the van Cittert-Zernike theorem to the imaging of incoherent synchrotron radiation with a pinhole. As a result of our analysis, we have provided an exact expression for the point spread function, which can be factorized as the product of two one-dimensional line spread functions. Using simple analytical expressions, we derived design formulas for a rectangular pinhole camera and calculated its resolution. As a practical application, we proposed a diagnostic beamline based on a magnetic chicane to measure the transverse electron beam size at ultralow-emittance machines with a pinhole camera. Operating at high photon energies ( $\sim 200\text{--}300$  keV) and

applying spectral filtering with a 4-mm-thick lead plate allows one to maximize spatial resolution, resulting in a point spread function width of approximately 13.7  $\mu\text{m}$ . We conclude our paper with estimates of the photon flux and demonstrate sufficient photon flux for effective imaging using the pinhole camera.

## ACKNOWLEDGMENTS

We thank Serguei Molodtsov and Kai Bagschik for their interest in this work. We thank Andreas Koch for the discussion on possible detector design.

- [1] D. Einfeld, J. Schaper, and M. Plesko, Design of a diffraction limited light source (DIFL), in *Proceedings of the Particle Accelerator Conference, Dallas, TX, 1995* (IEEE, New York, 1995), pp. 177–179.
- [2] C. G. Schroer, R. Roehlsberger, E. Weckert, R. Wanzenberg, I. Agapov, R. Brinkmann, and W. Leemans, PETRA IV: Upgrade of PETRA III to the ultimate 3D x-ray microscope, Conceptual Design Report, Deutsches Elektronen-Synchrotron DESY, Hamburg, Report No. PUBDB-2019-03613, 2019, <https://dx.doi.org/10.3204/PUBDB-2019-03613>.
- [3] C. Abraham *et al.*, Diamond-II Conceptual Design Report (2019), <https://www.diamond.ac.uk/dam/jcr:ec67b7e1-fb91-4a65-b1ce-f646490b564d/Diamond-II-ConceptualDesignReport.pdf>.
- [4] P. Raimondi *et al.*, The extremely brilliant source storage ring of the European Synchrotron Radiation Facility, *Commun. Phys.* **6**, 82 (2023).
- [5] R. Khubbutdinov, A. P. Menushenkov, and I. A. Vartanyants, Coherence properties of the high-energy fourth-generation x-ray synchrotron sources, *J. Synchrotron Radiat.* **26**, 1851 (2019).
- [6] G. Geloni, S. Serkez, R. Khubbutdinov, V. Kocharyan, and E. Saldin, Effects of energy spread on brightness and coherence of undulator sources, *J. Synchrotron Radiat.* **25**, 1335 (2018).
- [7] P. Li, M. Allain, T. A. Grünwald, M. Rommel, A. Campos, D. Carbone, and V. Chamard, 4th generation synchrotron source boosts crystalline imaging at the nanoscale, *Light Sci. Appl.* **11**, 73 (2022).
- [8] H. N. Chapman, Fourth-generation light sources, *Int. Union Crystallogr.* **10**, 246 (2023).
- [9] C. Thomas, G. Rehm, I. Martin, and R. Bartolini, X-ray pinhole camera resolution and emittance measurement, *Phys. Rev. ST Accel. Beams* **13**, 022805 (2010).
- [10] P. Elleaume, C. Fortgang, C. Penel, and E. Tarazona, Measuring beam sizes and ultra-small electron emittances using an x-ray pinhole camera, *J. Synchrotron Radiat.* **2**, 209 (1995).
- [11] M. Tordeux, L. Cassinari, O. Chubar, J.-C. Denard, D. Pédeau, and B. Pottin, Ultimate resolution of soleil x-ray pinhole camera, in *Proceedings of the 8th European Workshop on Beam Diagnostics and Instrumentation for Particle Accelerators, DIPAC 2007, Venice, Italy* (CERN, Geneva, Switzerland, 2007).

- [12] S. Takano, Beam diagnostics with synchrotron radiation in light sources, in *Proceedings of the International Particle Accelerator Conference, IPAC 2010, Kyoto, Japan* (ICR, Kyoto, 2010).
- [13] O. Chubar and P. Elleaume, Accurate and efficient computation of synchrotron radiation in the near field region—INSPIRE, in *Proceedings of the 6th European Particle Accelerator Conference, EPAC 1998, Stockholm* (IOP, London, 1998).
- [14] O. V. Chubar, Precise computation of electron-beam radiation in nonuniform magnetic fields as a tool for beam diagnostics, *Rev. Sci. Instrum.* **66**, 1872 (1995).
- [15] S. Kongtawong, O. Chubar, and T. Shaftan, Simulation of synchrotron radiation from electron beams affected by vibrations and drifts, *Phys. Rev. Accel. Beams* **25**, 024601 (2022).
- [16] G. Geloni, E. Saldin, E. Schneidmiller, and M. Yurkov, Statistical optics approach to the design of beamlines for synchrotron radiation, [arXiv:physics/0603269](https://arxiv.org/abs/physics/0603269).
- [17] G. Kube, Review of synchrotron radiation-based diagnostics for transverse profile measurements, in *Proceedings of the 8th European Workshop on Beam Diagnostics and Instrumentation for Particle Accelerators, DIPAC 2007, Venice, Italy* (CERN, Geneva, Switzerland, 2007).
- [18] M. Labat, O. Chubar, J. Breunlin, N. Hubert, and A. Andersson, Bending magnet synchrotron radiation imaging with large orbital collection angles, *Phys. Rev. Lett.* **131**, 185001 (2023).
- [19] M. Siano, B. Paroli, M. Potenza, L. Teruzzi, U. Iriso, A. Nosych, E. Solano, L. Torino, D. Butti, A. Goetz, T. Lefevre, S. Mazzoni, and G. Trad, Two-dimensional electron beam size measurements with x-ray heterodyne near field speckles, *Phys. Rev. Accel. Beams* **25**, 052801 (2022).
- [20] S. Serkez, Design and optimization of the grating monochromator for soft x-ray self-seeding FELs, Ph.D. thesis, Verlag Deutsches Elektronen-Synchrotron, 2015, No. PUBDB-2015-04348.
- [21] I. Agapov, G. Geloni, S. Tomin, and I. Zagorodnov, OCELOT: A software framework for synchrotron light source and FEL studies, *Nucl. Instrum. Methods Phys. Res., Sect. A* **768**, 151 (2014).
- [22] A. Trebushinin, G. Geloni, Y. Rakshun, and S. Serkez, Gaussian random field generator for simulating partially coherent undulator radiation, *Optica* **9**, 842 (2022).
- [23] J. W. Goodman, *Statistical Optics*, 2nd ed. (Wiley, Hoboken, NJ, 2000).
- [24] P. H. van Cittert, Die Wahrscheinliche Schwingungsverteilung in Einer von Einer Lichtquelle Direkt Oder Mittels Einer Linse Beleuchteten Ebene, *Physica (Utrecht)* **1**, 201 (1934).
- [25] F. Zernike, The concept of degree of coherence and its application to optical problems, *Physica (Utrecht)* **5**, 785 (1938).
- [26] J. Goodman, Some effects of target-induced scintillation on optical radar performance, *Proc. IEEE* **53**, 1688 (1965).
- [27] W. H. Carter and E. Wolf, Coherence and radiometry with quasihomogeneous planar sources, *J. Opt. Soc. Am.* **67**, 785 (1977).
- [28] Here we looked at the argument  $\xi$  of Eq. 5.44 in [29] and estimated at which angle the intensity drops to half its value, which gives  $y(\frac{3}{2}(\gamma\psi)^2) = 0.7$ , resulting in an exact value of  $\sigma_r = 0.22/\gamma$ , see Fig. 6.12 in [29].
- [29] P. J. Duke, *Synchrotron Radiation: Production and Properties*, Oxford Series on Synchrotron Radiation Vol. 3 (Oxford University Press, Oxford, 2000).
- [30] T. Tanaka and H. Kitamura, SPECTRA: A synchrotron radiation calculation code, *J. Synchrotron Radiat.* **8**, 1221 (2001).
- [31] A. Koch, Discussion on the possible design of the detector (personal communication).